

Melt Electrospinning for the Production of Osteochondral Scaffolds with Functional and Compositional Gradients

Gonçalo Nunes da Silva Carvalhão
goncalonscarvalho@gmail.com

Instituto Superior Técnico, Lisbon University
November 2016

The creation of functionalized materials offers the advantage of chemically tailoring surfaces that are useful for tissue engineering (TE). For that purpose, the processing technique to produce such structures must be precise enough in order to recreate the topographical geometry of living tissues.

Bearing in mind the need for this controlled surface engineering, it is hereby described the production of poly(ϵ -caprolactone) scaffolds through melt electrospinning materials functionalized with cell-binding peptides and antifouling polymer for the creation of gliding surfaces.

A hyaluronic acid-binding peptide (HA-BP) was synthesized using manual Fmoc solid-phase peptide synthesis, conjugated to PCL and processed by melt electrospinning to produce scaffolds. The same procedure was performed for another cell adhesion peptide, cRGDS. For polymer functionalization of materials, PCL was modified with an activators regenerated by electron transfer atom transfer radical polymerization (ARGET ATRP) initiator that was then melt electrospun and post-polymerized to create a poly(oligo(ethylene glycol) methacrylate) (pOEGMA) bottle-brush system through ARGET ATRP.

The presence of the functionalization elements on PCL surfaces was confirmed and the production of fibres was optimized to produce scaffolds aiming at the creation of platforms with different degrees of cell adherence.

Gliding and cell-adhesive surfaces such as those found in synovial joints, and cartilage and bone, respectively, are of great potential for the demanding therapeutic procedures and regeneration for osteochondral injuries.

Keywords: Melt electrospinning optimization, peptide-material functionalization, polymer-material functionalization, pOEGMA bottle-brushes, polymer brushes, surface-initiated ARGET ATRP.

INTRODUCTION

Osteochondral tissues are those that form the synovial joints, namely cartilage and bone, including elbow, knee, ankle and shoulder joints. Furthermore, it is an interfacial tissue that is extended from the superficial cartilage to the underlying subchondral bone and, as such, is composed of hierarchical stratified zones.¹

It is then possible to understand the several complexities that this interfacial tissue comprises and the difficulty towards their regeneration. Beyond these histological complexities, the difficulty in producing constructs for osteochondral regeneration is exacerbated by the avascular, aneural and alymphatic character of cartilage which leads to its limited reparative properties when damaged. Bone, on the other hand, is a vascularized tissue with a nerve supply and constantly remodels through equilibrium between the deposition of new bone and resorption of the extracellular matrix (ECM) by osteoblasts and osteoclasts, respectively.² Despite this advantageous characteristic, large bone defects, as observed after bone tumour resections and severe non-union fractures, lack the template for an orchestrated regeneration and are not able to heal for themselves.³

The biomechanical purpose of synovial joints is to provide lubricated contact between the moving surfaces with as little frictional forces as possible, which is achieved by separating the cartilage layers by a thin film of fluid, the synovial fluid.² This fluid and its producer, the synovial membrane, then form the gliding surfaces responsible for lubrication. These specialized surfaces are delicate and can be easily disrupted through trauma, infection or inflammation. In turn, this may lead to the formation of scar tissue – adhesions – that result from cellular ingrowth and bridging between previously gliding surfaces, leading to the restriction of movement and, hence, causing pain and compromised function. On the other hand, cell-adhesion is a prerequisite for their subsequent proliferation and differentiation and, hence, for tissue regeneration.⁴

In light of the obstacles found in osteochondral tissues, the design

of layered structures with both cell-adhesion (for tissue healing) and antifouling surfaces (to reduce cell ingrowth and allow the mobility between tissues) on opposing surfaces of scaffolds in a controlled fashion is extremely interesting for these tissues' regeneration.

Moreover, the modulation of characteristics such as roughness, porosity, chemical and biological composition allows the regulation of material integration within the body as well as the guidance of specific responses, such as cell adhesion, detachment, proliferation, differentiation, or metabolic activity.⁵

Peptide^{6,7,8} and polymer-functionalized⁸ polymeric material fibres have been produced and shown to promote several levels of cell-adhesion. For instance, Gentsch *et al.* 2011⁷ demonstrated that solution electrospinning of polymer-peptide conjugates containing the canonical adhesion sequence RGDS resulted in RGDS-functionalized poly(lactic-co-glycolic acid) (PLGA) scaffolds. This scaffolds showed the enrichment of the peptide motif on the PLGA scaffold's surfaces and improved cell adhesion and migration of murine fluorescent kidney fibroblasts when compared to fibres of the material alone. Furthermore, Harrison *et al.* 2015⁸ showed that the conjugation of the cyclised version of RGDS motif, cRGDS, with poly(ϵ -caprolactone) (PCL) also resulted in the production of surface-enriched electrospun scaffolds in the same motif, showing cell-adhesion of bovine tenocytes. The group included this design in a bilayer scaffold with an opposing antifouling surface enriched in Poly[oligo(ethylene glycol) methyl ether methacrylate] (pOEGMA) bottle-brushes, known for their antifouling properties. Indeed, this functionalization resulted in minimal adhesion by the same cells.

In addition to being able to substitute for ECM proteins, short peptide sequences supply a less system variability than naturally derived proteins and, when considering synthetic sequences, they are simple to graft to a surface by introducing a range of functional groups.⁹ Therefore, short peptides are candidates for surface functionalization aiming at cell adhesion. The canonical peptide sequence used for cell adhesion is the arginine-glycine-aspartic acid, RGD. This general cell-adhesion sequence is widely found in

ECM proteins and recognized by integrins, transmembrane receptors that are bridges for cell-cell and cell-ECM interactions. *In vivo* studies performed in animal models have reported that implant materials coated with RGD containing peptides improve early bone formation around implants.^{10,11}

Another peptide, concerning cartilage engineering, is an hyaluronic acid-binding peptide (HA-BP) that specifically and non-covalently binds HA and is used in order to mimic the dynamic nature of native ECM and protein–glycosaminoglycans interactions. This peptide, of amino acid (aa) sequence RYPISRPRKR, was derived from the HA-binding region of the link protein which stabilizes the interaction between HA and the proteoglycan aggrecan in articular cartilage. In the work performed by Harrison *et al.* 2015⁸, pOEGMA bottle-brushes were achieved by ARGET ATRP polymerization of OEGMA. This technique is part of controlled radical polymerizations (CRP) that are versatile and facile methods for surface functionalization, as most compounds with double bonds may be incorporated into the polymer in the presence of almost any other functional group.¹² Regarding the material for the bulk scaffold, polymers are of great interest in the area of TE, since they can be both bioactive and biodegradable and their properties such as mechanical strength can be tailored.¹³

Natural polymers, of which hyaluronic acid and collagen are examples, are interesting options for TE since they provide innate biological information to cells so as to guide them towards cell attachment and chemotactic responses. These polymers are, however, limited in sourcing, potentially prone to disease transmission, poorly handled and possess weak mechanical properties.³ Regarding synthetic polymers, although they lack the innate biological information guidance to cells, they are often chosen over natural ones since they are flexible in being processed, easily tailored chemically and capable of degradation, with better lot-to-lot consistency¹⁴. Indeed, degradation of synthetic polymers such as poly(lactic acid) (PLA), poly(glycolic acid) (PGA), and poly(ϵ -caprolactone) (PCL) produces monomers which are quickly removed by the natural physiological pathway. This allows, for instance, for osteoblasts to produce and substitute that volume with natural mineralization.¹⁵

There are several methods extensively studied for the manufacturing of porous scaffolds, such as chemical/gas foaming¹⁶, solvent casting and particulate leaching^{17,18}, freeze-drying^{19,20}, thermally induced phase separation^{21,22,23}, fibre meshing²⁴ and sol-gel²⁵. However, these techniques do not allow the control of pore size, shape and its interconnectivity.²⁶

Aiming at overtaking these limitations, additive manufacturing (AM) approaches such as 3D printing (3DP), solid freeform fabrication (SFF), rapid prototyping (RP). AM is a broad term for an increasing number of techniques in which complex structures are constructed in a layer-by-layer fashion according to computer aided design (CAD).²⁷ Each layer can be built to have a specific morphological configuration to achieve the desired micro and macrostructure of the scaffold. TE benefits from AM the possibility of manufacturing custom-shaped implants with controlled internal and external architecture based on medical imaging data.²⁸ However, these approaches are not able to achieve sub-micron

fibres that are characteristic of living tissues. Furthermore, although solution electrospinning (SE) can achieve this nanometric fibres, it recurs to organic solvents, with the volatility and toxicity issues associated,²⁹ and to electric fields that lead to a lack of control in fibre deposition, having limited reproducible geometry. This uncontrolled fiber deposition fashion then leads to small pore sizes, which act as a barrier to cell infiltration rather than promoting it^{30,31}. In this work, melt electrospinning, which shows a higher control over the deposition of fibers, is used. ME combines the cell-scale topographical features of SE electrospinning with the spatial control and geometrical complexity of fused deposition modelling (FDM)^{32,31}, by melting a polymer rather than using a polymer solution. Moreover, the higher viscosity and lower conductivity of melts when compared to solutions leads to a drastic decrease of whipping and other instabilities during the production of the fibres with voltage applied.²⁷ This, associated to a computer controlled-stage, allows for the fabrication of controlled deposition of polymeric fibres, making melt electrospinning more similar to other additive manufacturing technologies. Moreover, this technique was shown to achieve sub-micron average fibre diameters (AFD) by applying high electrical fields, low flow rates and small diameter spinnerets.³⁹

Bearing in mind the main obstacles in scaffold engineering, the main goal of this work is to produce geometrically-controlled and functionalized fibre meshes in order to promote several levels of cellular adhesion needed as tools for TE, with focus on osteochondral lesions.

In order to do that, peptide and polymer bottle-brushes were fabricated so as to functionalize the surface of melt electrospun PCL scaffolds.

The first part of the project consisted in producing the decorative motifs promoting cell adhesion – peptides – and promoting the creation of gliding surfaces with pOEGMA bottle-brushes, avoiding this feature.

For the peptide functionalization of the PCL polymer, the hyaluronic acid binding-peptide (HA-BP) and a cyclised version of RGD, cRGDS, both used previously by the group with SE (Chow *et al.* 2014⁶ for the HA-BP and Harrison *et al.* 2015⁸ for cRGDS) were chosen. This version of the RGD peptide, cRGDS, was used as it has long been recognized that the RGD sequence loses affinity and specificity when presented outside the context of the native protein.^{35,36} The activity of the sequence can be improved by adding surrounding amino acids (aa) from the native sequence³⁷, and by cyclizing the peptide, as this is most likely to exist in an exposed loop conformation in ECM proteins such as fibronectin.^{38,39}

After synthesized recurring to Fmoc SPPS, these peptides were conjugated to low molecular PCL. In order to produce the peptide-polymer conjugates, the peptides comprised the bioactive sequence (cRGDS and HA-BP) and a CGGG (a cysteine, and three glycines) so as to link the bioactive sequence to the biomaterial. The glycines served as spacers and the cysteine on the N-terminus was coupled to the PCL by reacting the thiol side chain of the cysteine with the maleimide group of the linker molecule, p-maleimidophenyl isocyanate (PMPI), in a Michael-type addition.⁴⁰

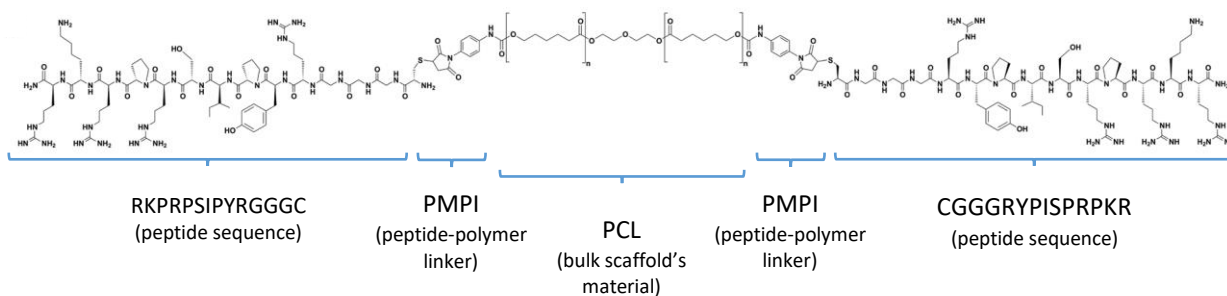


Figure 1 - Chemical structure of the hyaluronic acid – binding peptide (HA-BP) – PCL conjugate with the specific binding sequence RYPISRPRKR. Adapted from Chow *et al.* 2014⁶.

The representation of the final peptide-polymer conjugates in the case of HA-BP is shown in Figure 1. It is worth noting that the reaction occurs in both ends of PCL chains and that low MW PCL (M_w 14 000) was selected to prevent water solubility of the conjugates and affectively anchor them to the bulk fibres.⁶

MATERIALS AND METHODS

Peptide synthesis and purification

The 14-aa peptide sequence (CGGGRYPISRPKR) was synthesized by manual Fmoc solid-phase peptide synthesis (SPPS), using a 50 mL peptide synthesis vessel (Synthware Glass) and a nitrogen-bubbling system (Schlenk line). Fmoc-Rink-Amide aminomethyl polystyrene resin (100-200 mesh, 0.56 mmol/g functionalization) the solid support for the synthesis, Fmoc-protected aa and Benzotriazole-N,N,N',N'-tetramethyluronium-hexafluorophosphate (HBTU), the coupling agent, were purchased from AGTC Bioproducts (UK), as well as diisopropylethylamine (DIPEA) and dithiothreitol (DTT). Solvents, dimethyl formamide (DMF) and dichloromethane (DCM) were purchased from Honeywell (Sweden). Trifluoroacetic acid (TFA), triisopropyl silane (TIS) and Piperidine purchased from Sigma Aldrich (Sweden). All reagents were synthesis-grade. The protocol used was adapted from Chow *et al.* 2014⁶ for a 0.25 mM scale. Firstly, the resin was swollen for 30 min in DCM and deprotected by a 20% Piperidine in DMF solution and then washed with DCM and DMF. Each aa was, then, coupled to the growing peptide sequence by adding an activated solution of HBTU and DIPEA (3.95 and 6 eq., respectively, to 4 eq. of aa) for 1h30. After each deprotection and coupling, and to confirm if each of these steps worked, Nihydrin tests (NT, Kaiser tests) purchased from Sigma were performed at 100 °C to assess the presence of free amines. After finishing the peptide sequence, following the Fmoc-deprotection of the last aa, the peptide was cleaved from the resin for 4h recurring to a 95% TFA, 2.5% TIS, 2.5% of Millipore water with 2.5% (w/v) of DTT solution. TFA was, after recovery of the cleaving solution plus the peptide, removed by rotary evaporation.

In order to recover and perform an intermediate purification, the peptide residue solution was precipitated with cold diethyl ether (DEE) and washed with DEE and Millipore water to allow the removal of residual aa and other reagents. After new washings with DEE, the precipitate was dried using a Nitrogen line and then let completely dry overnight in a vacuum desiccator until the polishing step. In the purification step, the peptide was dissolved in a solution of 5% acetonitrile (ACN, AGTC Bioproducts), 0.1% TFA and ultrapure water, which was passed through a 0.45 µm filter and injected into a reverse phase preparative high performance liquid chromatography (HPLC). The HPLC was performed by running a mobile phase gradient of 95% ultrapure water and 5% ACN to 100% ACN with 0.1% TFA. Lastly, the solution containing the purified peptide was rotary evaporated, frozen to -80°C and freeze dried. cRGDS peptide was kindly prepared and purified by Dr. Paresh Parmar (Stevens Group, Imperial College London, UK) using the same methodology.

Peptide – PCL conjugation

To prepare the conjugates, the terminal hydroxyl groups of PCL (M_w 14 kDa) were modified with PMPI to generate a maleimide-functionalized PCL. The peptides were, then, coupled to the PCL-maleimide by reacting the thiol side chain of the cysteine with the maleimide group via Michael type addition.

In this scheme for the conjugation, an adapted protocol from Chow *et al.* was used. In brief, PCL (Sigma, M_w 14 kDa) was dissolved in anhydrous DMF at 250 mg/mL in a round bottom flask previously covered and sealed with a rubber septum. The solvent was added recurring to a syringe with a long needle and a nitrogen line with exhaustion needles to keep the pressure of the round bottom flask positive and prevent the entrance of water as the reaction of the PCL with PMPI can't be performed in its presence. The dissolution

of the PCL in the solvent was promoted by adding a small stir bar and by sonicating the solution.

After complete dissolution, p-maleimidophenyl isocyanate (PMPI, Chem-Impex International, Inc.) at 15-fold molar excess to PCL was dissolved in anhydrous DMF and added drop-wise to the PCL solution. The resulting solution was bubbled with nitrogen for 15 minutes and was allowed to react under low stirring rate over night. At the end of the reaction, the conjugation reaction was confirmed by ¹H NMR and the product was precipitated and washed with cold DEE and then with water to remove the excess of unreacted PMPI. Finally, the purified product in water was frozen to -80°C, freeze-dried and stored in the cold room.

For both cRGDS and HA-BP, the purified peptides and PCL-PMPI were dissolved in anhydrous DMF separately with a 4 molar excess of peptide. Each peptide was then added to the PCL-PMPI solution a let react over low stirring overnight. The resulting conjugates were precipitated and washed with cold DEE and washed with water to remove the excess of peptide and then dried under vacuum.

Assessment of HA-BP and cRGDS in the melt electrospun fibres's surface

The functionality of biotinylated HA-BP in the final melt electrospun fibres was assessed visually by binding HA-fluorescein isothiocyanate (FITC). Samples were first blocked in 0.1% (w/v) bovine serum albumin (Sigma Aldrich) in PBS, followed by 0.5 mg/mL FITC-HA (Millipore, Sweden) in PBS for 1h at 37°C. Samples were washed in PBS to remove unbound FITC-HA and imaged on a Zeiss Axio Imager M2 upright epifluorescent microscope, relative to unfunctionalised and cRGDS-functionalized controls.

End functionalization of PCL with polymerization initiator

PCL-diol (50% w/w 45-80 kDa) was functionalized with the polymerization initiator BiBB using a protocol adapted from literature⁸ to produce PCL-Ini.

Briefly, to produce 1 g of the PCL-Ini (17% (w/w) BiBB), 830 mg of a 50% 45kDa-80kDa PCL blend (Sigma Aldrich) was diluted in 4 mL of anhydrous tetrahydrofuran (THF) in a glass vessel until complete dissolution. Afterwards, 170 mg of BiBB was added into the vessel and the reaction was let to react over night at room temperature. Finally, the final reaction mixture was reduced through vacuum rotary evaporation and precipitated into DEE and dried in a vacuum drier.

Development of a biotinylated monomer for production of p(OEGMA-co-biotin)

A 0.30 mM scale of biotinylated PEG monomer was synthesized by manual Fmoc-SPPS, as described in Harrison *et al.* 2015⁸, and using the same equipment as for the HA-BP synthesis. Common reagents to both synthesis were purchased from the same distributors, unless otherwise stated. Succinctly, after swelling of the resin with DCM, it was deprotected and coupled to Fmoc-Lys(Mtt)-OH (4 eq., 2h).

As for the removal of the Mtt group, a solution of 1.5% (v/v) TFA in DCM was used to wash the resin (2x 15 min). The resin was further washed with DIPEA in DMF 1% (v/v) and DCM after which methacryloyl chloride (8 eq., 10 min) in DCM was coupled to the free amine. Three units of Fmoc-O2Oc-OH (2 eq., 3 h) were then coupled to the resin, followed by a biotin group after the final fmoc deprotection. All couplings were performed with HBTU (4 eq.) and DIPEA (8 eq.). The monomer was cleaved from the resin with a cocktail of TFA / triisopropyl silane / H₂O (95/2.5/2.5 v/v/v, 2 h), precipitated in DEE and purified by HPLC (C18 column, H₂O / acetonitrile gradient).

OEGMA polymerization in solution and from 2D and 3D PCL-initiated structures

The protocol followed, adapted from Harrison *et al.* 2015⁸, consists in three major procedures: removal of inhibitors from the OEGMA monomer, ARGET ATRP reaction and termination of the reaction.

The first step was performed by creating a column with a 20 mL syringe, filled 1/20 with cotton wool (to act as a filter), 7/20 with basic aluminium oxide purchased from Sigma Aldrich and 8/20 with inhibitor removal beads. Poly(ethylene glycol) monomethyl ether monomethacrylate (OEGMA) purchased from Polysciences (Germany) with a Mn of the poly(ethylene glycol) unit of 400 Da was then allowed to gravity filter through the column and aliquots were frozen at -20 °C until use.

The ARGET ATRP reaction was performed in a glass flask (the reaction vessel) on ice, OEGMA (227 mg, 0.7 mmol, Polysciences, Germany), copper (II) chloride (Cu(II)Cl₂, 0.42 mg, 0.0047 mmol), tris[(2-pyridyl)methyl]amine (TPMA, 1.37 mg, 0.0047 mmol), and ethyl α -bromoisobutyrate (EBiB, 0.92 mg, 0.0047 mmol) were added in 2 mL of 50% (v/v) isopropyl alcohol (IPA) aqueous solution. The vessel was then sealed and degassed with nitrogen for 30 min. An ascorbic acid solution (AscA 0.08 mg, 0.00047 mmol) was also degassed with nitrogen for 30 min and then added to the reaction with a syringe. The reactor was covered in aluminium foil, placed into a pre-warmed water bath at 31°C and let react for 2h. After this time, the reaction was stopped by exposing the reaction to oxygen and confirmation of polymerization was assessed by size exclusion chromatography (SEC) using a 1260 Infinity Binary LC System (Agilent Technologies, UK).

Assessment of the p(OEGMA-co-biotin) polymer brushes on PCL-initiated printed scaffolds

The FITC-streptavidin protocol followed was adapted from Harrison et. al 201547 and started by the blocking of the p(OEGMA-co-biotin) polymerized scaffolds with a 1% (w/w) bovine serum albumin (BSA) and 0.1% (w/v) tween 20 in PBS solution for 30 minutes. Afterwards, the samples were stained for 15 minutes with fluorescein-streptavidin diluted to 1 μ g/mL in 1% (w/w) BSA in PBS at pH 8.4 and washed three times with PBS. The samples were imaged on a fluorescence microscope Axio Imager M2 (Zeiss).

Preparation of the PCL blends for melt electrospinning

45 kDa (Mn = 45 000) and 80 kDa (Mn = 80 000) poly- ϵ -caprolactone (PCL) were purchased from SigmaAldrich Co. LLC. In order to print the PCL fibers, a blend 50/50 (w/w) was made by dissolution of both MW PCL in chloroform (20% w/v), purchased also from SigmaAldrich, in a glass flask under moderate stirring. After complete dissolution (approximately 1h), the solvent was removed under nitrogen and vacuum drying. The blend was then loaded into a syringe and heated (85 °C, 5 mbar) before processing by MEW.

Production of non-functionalized and functionalized PCL fibres by MEW

PCL fibres were produced using a direct writing melt electrospinner engineered by the Hutmacher Laboratory (Queensland University of Technology, Australia). The movement of the stage was controlled using CNC software Mach3 Mill (Arsoft), which controls the motion of two stepper motors by processing a G-code program.

Optimization of the diameter and geometry deposition of fibres by MEW

For this optimization, five different pressures (0.12-0.30 MPa, in 0.03 MPa intervals) and five different collector plate speeds (500-1500 mm/min, in 250 mm/min intervals) were tested and the other parameters (temperature, T, and high voltage, HV) were kept constant (T = 75 °C, HV = 8 kV). In order to perform these tests in an efficient and uniform way, a G-code comprising five collector plate speeds was created and run for each pressure value. The G-code was designed in order to print in two distinct areas: a stabilization area and a testing area. As the melt electrospinner starts printing with a new condition, the equipment needs time to reach stationary phase and print uniform fibers. Therefore, the program starts with the stabilization of the fibers by printing them in 80 passes in a part of the collector plate and then moves to the printing area to print in 8 passes in the testing area. These last fibers

were the ones imaged and measured recurring to the fluorescence microscope.

Production of non-functionalized and functionalized PCL scaffolds by MEW

3x3 cm orthogonal grid scaffolds with 500 μ m fibre spacing and 30 double layers were produced using an appropriate G-code.

RESULTS AND DISCUSSION

Peptide functionalization

In order to prove PCL surface-functionalization with the peptides, these and a PCL control were stained with HA – fluorescein. After the washing step, which washes out the HA that wasn't bind to the peptides on the surface, scaffolds were imaged using fluorescent microscopy. Since HA – BP specifically binds to HA (it's derived from the HA-binding region of the link protein) and RGDS is a general cell-adhesion sequence, it is expected that the fluorescence intensity increases in the order, PCL control, PCL – cRGDS and PCL – HA – BP.

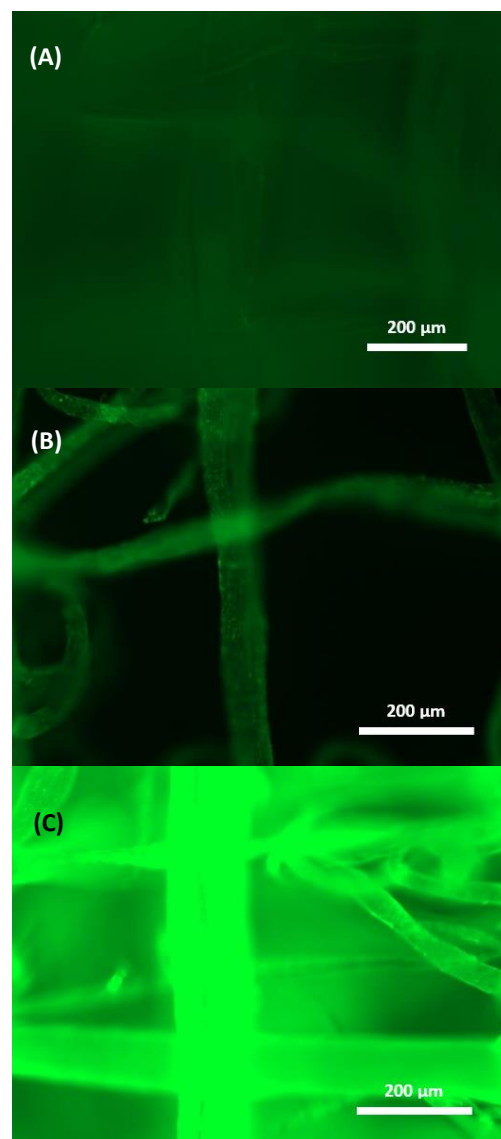


Figure 2 – Fluorescence micrographs of PCL control (A), PCL-cRGDS (5% (w/w)) (B) and PCL-HA-BP (5% (w/w)) (C) with HA – fluorescein labelling (10x).

In Figure 2 (A), one can observe that this PCL scaffold is showing minor auto fluorescence and negligible non-specific binding of HA-FITC, as there are not specific fluorescence sites. Regarding Figure 2 (B), the localized fluorescence on the fibres is more pronounced, indicating some non-specific binding to the charged cRGDS peptide. The HA – BP scaffold in Figure 2 (C) shows a significantly greater

fluorescence intensity, indicating that the surface was successfully enriched in functional HA-binding peptide. The difference in intensity between the cRGDS and HA-BP scaffolds indicates that the HA-FITC binds with greater affinity to the HA – BP sequence.

Polymer functionalization

ARGET ATRP polymerization in solution and polymer brush grafting from PCL-initiated surfaces and from electrospun fibers were performed using the optimized reaction conditions found in Harrison *et al.* 2015. A typical polymerization (Figure 10, (A) – (C), Appendix I) achieved approximately $M_n = 30\,000$, $M_w = 40\,000$ and dispersity 1.2-1.3.

In addition to the analysis of the free polymer in the reaction vessels, the presence of the polymer brushes were assessed using fluorescent labelling. The biotinylated PEG monomer was successfully polymerized together with OEGMA to produce p(OEGMA-co-biotin). The post-polymerized fibres (PCL control and PCL-Ini) were then labelled with fluorescein-streptavidin and the images collected from fluorescent microscopy are displayed in Figure 2.

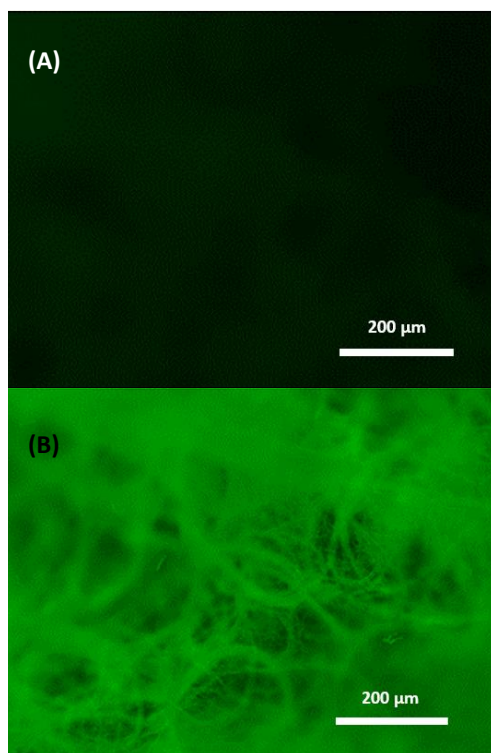


Figure 3 – Fluorescence micrographs of PCL-Ini (A) and PCL-p(OEGMA-co-biotin) FITC-streptavidin labelling (10x).

The image shown in Figure 3 (B), a section of the p(OEGMA-co-biotin) scaffold, show clear fluorescein conjugation when

compared to the auto fluorescence of PCL-Ini scaffold shown in the same figure (A), which again corroborates the validation of the bottle-brush system.

Melt electrospinning

Melt electrospun fibre optimization

To our knowledge, although there is an optimization for the AFD of 50 kDa PCL, there is no optimized standard operating procedure (SOP) that correlates the conditions used in ME with the resulting geometry deposition of fibres neither with their resulting diameter for this 50% 45-80 kDa PCL blend. This way, with the purpose of creating a general protocol for the production of scaffolds with tailorable of both fibre geometry deposition and fibre diameter, the protocol described in the material and methods section was followed. After collecting the resulting 50% (w/w) 45-80 kDa PCL fibres, the samples were imaged using the bright field of the fluorescence microscope. For each amplification, two micrographs were taken and the ones showing the four extreme conditions of pressure and collector plate speed used are presented in Appendix II, in Figure 11. 10x micrographs were used to understand the geometry of fibres deposition and 40x micrographs were used for the measurement of the fibre diameters, for more accurate results. The geometry of fibre deposition was also analysed and is presented in Appendix III.

By analysing Figure 11, one can conclude that for the highest collector speed rate, the fibres are deposited as straight lines (Figure 11 C,D,G,H) and, for the lowest values of this parameter, the fibres are deposited in a wave-like pattern (Figure 11 A, B, E, F), independently of the range of pressures tested. Moreover, Table 1 present in appendix II shows that for collector speeds rates between 500 and 750 mm/min the geometry for fibre deposition happens in a wave-like pattern and that for speeds between 1000 and 1500 mm/min the geometry turns into a linear fashion. In order to obtain coil-like patterns, the speeds applied should had been significantly lower.

Two assays were performed for each temperature and pressure and three diameter measurements were performed per assay, resulting in a total of six measurements. After measuring the diameter of the fibres, the AFD was estimated and the standard deviation for the six values for each condition was calculated. These results can be found in Table 2, present in Appendix III.

The AFD values were then plotted in a graphic (Figure 4) against the pressure with their respective error for each set of collector speeds. A trend-line was added and the mathematical relationship between P and AFD (with the correlation coefficient, R) was found in the form of $AFD = mP + b$, where m and b are the slope of the curve and b the y-intercept value.

As expected⁴¹, the biggest AFD value was achieved with the highest pressure and lowest collector speed rate. Conversely, the lowest AFD value was achieved with the lowest pressure and highest collector speed rate.

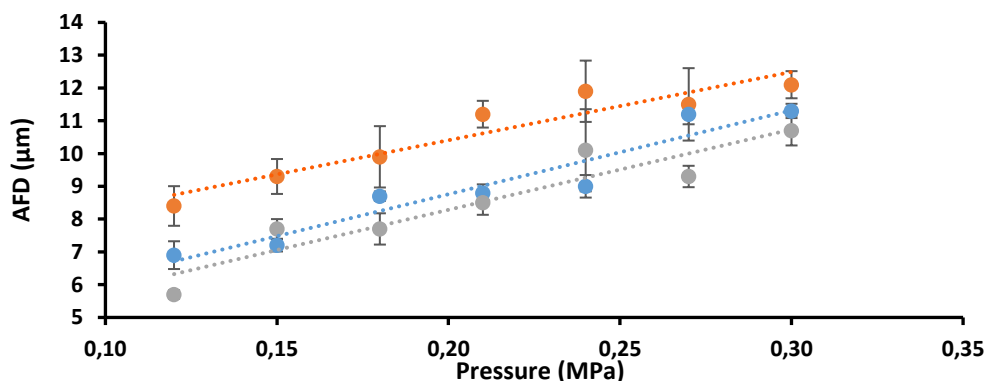


Figure 4 – Graphical representation of the influence of pressure and collector speed in the AFD of melt electrospun PCL fibres ($T = 70\text{ }^{\circ}\text{C}$). After linearization of the data for each collector speed rate, AFD is given for 500 mm/min: $AFD_{500} = 20.8P + 6.2$, $R^2 = 0.90$; for 1000 mm/min: $AFD_{1000} = 25.8P + 3.6$, $R^2 = 0.92$ and for 1500 mm/min: $AFD_{1500} = 24.5P + 3.4$, $R^2 = 0.88$.

This optimization study is important to know what conditions to use regarding P and S_C to obtain a specific AFD in the production of scaffolds using the 50% 45/80 kDa PCL blend.

Melt electrospinning writing for the production of functionalized scaffolds

The fabrication of PCL fibers and scaffolds was successful after qualitative optimization of parameters such as temperature, pressure and voltage. To our knowledge, this is the first instance of end-functionalized polymers processed by ME.

The 50% 45-80 kDa PCL blend was the one chosen for the peptide and initiator blends printing, as it displayed consistent printability, as shown in Figure 5.

After end-functionalizing 14 kDa PCL with the decorating peptides (PCL-HA-BP and PCL-cRGDS) and the polymerization initiator (PCL-Ini), 17% PCL-Ini, 5% PCL-cRGDS and 5% PCL-HA-BP in 50% 45-80 kDa PCL blends were produced and their printing into geometrically-controlled scaffolds was attempted through optimization of temperature, pressure and collector speed rate.

The printing of the PCL blend with the polymerization initiator, BiBB, as well as the operating conditions are shown in Figure 6. The produced scaffold seems to present several degrees of complexity that can be potentially important in mimicking the *in vivo* histology of tissues, as it can be seen larger fibers deposited perpendicularly in a mesh and smaller randomized fibers.

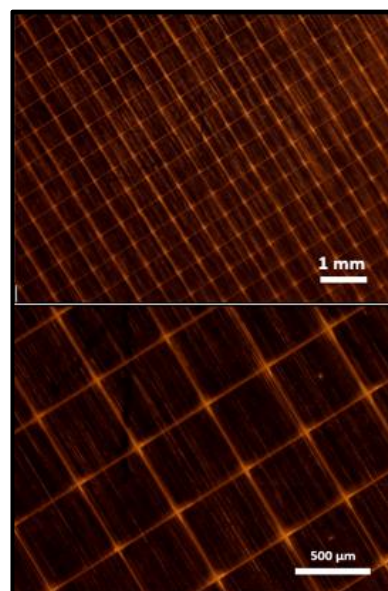


Figure 5 - USB microscope images of a 50% (w/w) 45-80 kDa PCL double-layered scaffold. Printing parameters: $T_{ring} = T_{tube} = 70^{\circ}C$, $P = 0.120$ MPa, speed = 1000 mm/min, HV = 8kV, PS=0.50 mm.

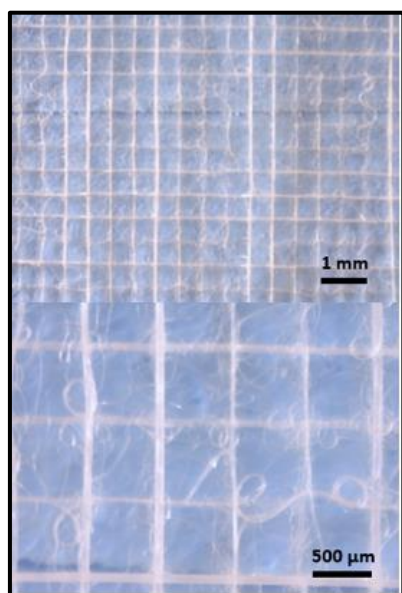


Figure 6 – USB microscope images of PCL-Ini 10 double-layered scaffolds with 17% (w/w) BiBB. Printing parameters: $T_{ring} = 90^{\circ}C$, $T_{tube} = 85^{\circ}C$, $P = 0.250$ MPa, speed = 1400 mm/min, HV=7kV, PS=0.50 mm.

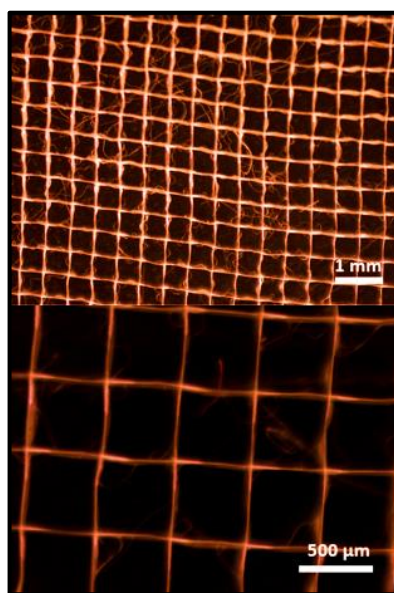


Figure 7 - USB microscope images of 30 double-layered scaffolds with 5% HA-BP in PCL. Printing parameters: $T_{ring} = 80^{\circ}C$, $T_{tube} = 85^{\circ}C$, $P = 0.250$ MPa, speed = 850 mm/min, HV=8kV, PS=0.50 mm.

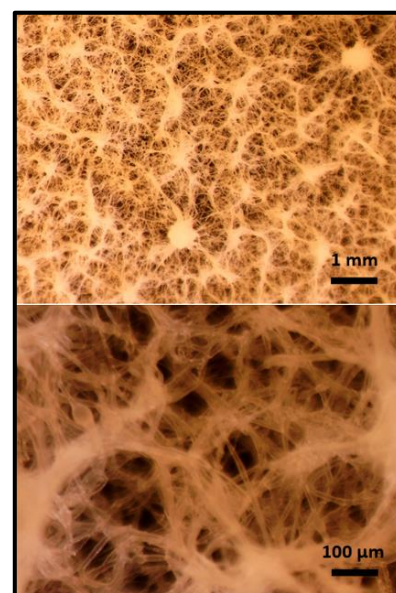


Figure 8 – USB microscope images of PCL with 5% (w/w) cRGDS. Printing parameters: $T_{ring} = 90^{\circ}C$, $T_{tube} = 85^{\circ}C$, $P = 0.250$ MPa, speed = 1400 mm/min, HV=7kV, PS=0.50 mm.

Figure 7 shows the structures of the fibres that compose the PCL-HA-BP scaffold obtained and this specific blend turned out to be the easiest to print, from the functionalized fibres. This is advantageous, as the scaffolds for cartilage regeneration benefit from smaller pore sizes, between 150 and 250 μm ⁴². Since this 500 μm spaced scaffold displays a consistent printability and since diminishing the pore size of a scaffold leads to the increase in the electric interactions between the molten filament being printed and the already printed fibres, which affects the control of fibre deposition, this blend shows potential to produce smaller pore-sized scaffolds as the ones needed for cartilage engineering.

Regarding Figure 8, it shows the PCL-cRGDS (5%) scaffold obtained. By observing this figure, one can notice that the fibres composing this scaffold are randomized instead of displaying an organized orthogonal grid mesh, in spite of the several attempts at optimizing

this blend by using pressures 0.20-0.30 MPa, HV 7-8 kV, speeds 850-1000 mm/min and temperatures ranging from 80 to 110 $^{\circ}C$. The pore size was kept at 0.50 mm so as to avoid the effect of scaffold geometry in future cell assays and, hence, was not increased in order to obtain consistent printability. Moreover, pore size in bone scaffolds are optimal for successful diffusion of nutrients and oxygen, vascularization and continuous ingrowth of bone tissue in the range of 200 to 350 μm .^{43,44,45}

During the printing process for this functionalized PCL, it was observed that the fibres produced weren't continuous and uniform. As a matter of fact, the flow coming out from the spinneret was frequently stopped by what it seemed to be small crystals, probably insoluble peptide, that were clogging the needle. For this reason, the speed of the collector plate could not be increased above 1000 mm/min in order to straighten the fibres, as this would only result

in the heterogeneous printing of this blend. Several attempts were made aiming at the dissolution of the crystals, namely the sonication of the PCL blend dissolved in chloroform. Another possible solution would be the complete re-dissolution of the blend in chloroform, followed by a filtration in order to remove the crystals, task that wasn't performed due to restrictions in time.

FINAL REMARKS AND FUTURE DIRECTIONS

This work allowed for the confirmation that ME can be used for the production of geometrically-controlled fibres composed of biofunctionalized PCL with polymers and peptides, as has been proved before with SE.^{8,6,7} Indeed, HA-BP and the canonical adhesion sequence cRGDS were successfully conjugated to PCL and located on the surface of PCL scaffolds after melt electrospinning. Also, PCL was successfully end-functionalized with the ARGET ATRP initiator, BiBB, and melt electrospun into scaffolds that were post-polymerized with ARGET ATRP on their surfaces.

Melt electrospinning technique was also optimized for the production of controlled diameter and geometry deposition of pure PCL fibres.

This work shows potential applications not only in osteochondral regeneration but in other fields of TE as the techniques used are versatile and capable of corresponding to the histological needs of different tissues.

Further work following this project would begin with the assessment of the cell adhesion and proliferation capacity of each functionalized scaffold with human mesenchymal stem cells (hMSCs), capable to differentiate into osteoblasts and chondrocytes, as cell adhesion is a key event for cell proliferation and differentiation, needed for regeneration of tissues.

Following this work, further cell assays should be performed to assess the differentiation capacity of each peptide-functionalized scaffold. This would hopefully show the enhanced differentiation of hMSCs into chondrocyte and osteoblastic lineages, in HA-BP and cRGDS functionalised scaffolds, respectively.

At the same with this experimental cell work, the printing of the functionalized blends should be further optimized to construct multi-layered scaffolds, which would be achieved by sequential ME of PCL-cRGDS (for the bone area), PCL-HA-BP (for the cartilage area) and PCL-p(OEGMA) (for the mobility of the joint). This way, a printing scheme as the one shown in Figure 9 could be attempted.

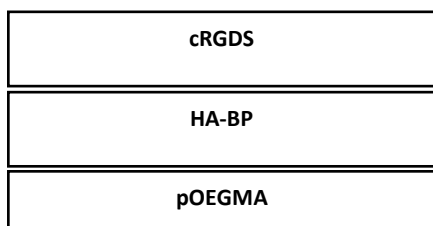


Figure 9 – Schematic representation of the idealised multi-layered osteochondral scaffold.

For accurate geometrical/histological recreation of osteochondral tissues, computed tomography from healthy patients could be used to obtain a CAD file with Materialise Mimics® software, for instance, and then this CAD file could be converted into G-code with Slic3r software, that would be used for ME printing of the osteochondral scaffold.

In sum, the systems here established will hopefully help to create efficient ways to ease the fabrication of porous scaffolds with appropriate biomimetic cues for osteochondral regeneration.

REFERENCES

1. Seo S-J, Mahapatra C, Singh RK, Knowles JC, Kim H-W. Strategies for osteochondral repair: Focus on scaffolds. *J Tissue Eng.* 2014;5(0):2041731414541850. doi:10.1177/2041731414541850.
2. McMahon L, O'Brien F, Prendergast P. Biomechanics and mechanobiology

- in osteochondral tissues. *Regen Med.* 2008;3(5):743-759. doi:10.2217/17460751.3.5.743.
3. Stevens MM. Biomaterials for bone tissue engineering. *Mater Today.* 2008;11(5):18-25. doi:10.1016/S1369-7021(08)70086-5.
4. Ducheyne P. *Comprehensive Biomaterials.* 1st ed. Elsevier Science; 2011.
5. Uquillas Paredes JA, Polini A, Chrzanowski W. Protein-based Biointerfaces to Control Stem Cell Differentiation. :1-29. doi:10.1039/9781782628453-00001.
6. Chow LW, Armgarth A, St-Pierre JP, et al. Peptide-directed spatial organization of biomolecules in dynamic gradient scaffolds. *Adv Healthc Mater.* 2014;3(9):1381-1386. doi:10.1002/adhm.201400032.
7. Gentsch R, Pippig F, Schmidt S, Cernoch P, Polleux J, Börner HG. Single-step electrospinning to bioactive polymer nanofibers. *Macromolecules.* 2011;44(3):453-461. doi:10.1021/ma102847a.
8. Harrison RH, Steele JAM, Chapman R, et al. Modular and Versatile Spatial Functionalization of Tissue Engineering Scaffolds through Fiber-Initiated Controlled Radical Polymerization. *Adv Funct Mater.* 2015;25(36):5748-5757. doi:10.1002/adfm.201501277.
9. Mager MD, LaPointe V, Stevens MM. Exploring and exploiting chemistry at the cell surface. *Nat Chem.* 2011;3(8):582-589. doi:10.1038/nchem.1090.
10. Germanier Y, Tosatti S, Broggin N, Textor M, Buser D. Enhanced bone apposition around biofunctionalized sandblasted and acid-etched titanium implant surfaces: A histomorphometric study in miniature pigs. *Clin Oral Implants Res.* 2006;17(3):251-257. doi:10.1111/j.1600-0501.2005.01222.x.
11. Kroese-Deutman HC, van den Dolder J, Spauwen PHM, Jansen J a. Influence of RGD-loaded titanium implants on bone formation in vivo. *Tissue Eng.* 2015;11(11-12):1867-1875. doi:10.1089/ten.2005.11.1867.
12. Hawker CJ, Wooley KL. The Convergence of Synthetic Organic and. *Science (80-).* 2005;309(August):1200-1206. doi:10.1126/science.1109778.
13. Lichte P, Pape HC, Pufe T, Kobbe P, Fischer H. Scaffolds for bone healing: Concepts, materials and evidence. *Injury.* 2011;42(6):569-573. doi:10.1016/j.injury.2011.03.033.
14. Olivares AL, Marsal È, Planell J a., Lacroix D. Finite element study of scaffold architecture design and culture conditions for tissue engineering. *Biomaterials.* 2009;30(30):6142-6149. doi:10.1016/j.biomaterials.2009.07.041.
15. Bose S, Roy M. Recent Advances in Bone Tissue Engineering Scaffolds. *Trends Biotechnol.* 2013;30(10):546-554. doi:10.1016/j.tibtech.2012.07.005.Recent.
16. Kucharska M, Butruk B, Walenko K, Bryn T, Ciach T. Fabrication of in-situ foamed chitosan/β-TCP scaffolds for bone tissue engineering application. *Mater Lett.* 2012;85:124-127. doi:10.1016/j.matlet.2012.07.002.
17. Szkodo M. Clay Minerals – Mineralogy and Phenomenon of Clay Swelling in Oil & Gas Industry. 2015:3-9. doi:10.1515/adms.
18. Zhu N, Chen X. Advances in Biomaterials Science and Biomedical Applications. In: *Advances in Biomaterials Science and Biomedical Applications.* INTECH; 2013:315-328. doi:10.5772/56420.
19. Sultana N, Wang M. Fabrication of HA/PHBV composite scaffolds through the emulsion freezing/freeze-drying process and characterisation of the scaffolds. *J Mater Sci Mater Med.* 2008;19(7):2555-2561. doi:10.1007/s10856-007-3214-3.
20. Seol Y-J, Lee J-Y, Park Y-J, et al. Chitosan sponges as tissue engineering scaffolds for bone formation. *Biotechnol Lett.* 2004;26:1037-1041. doi:10.1023/B:BILE.0000032962.79531.f.
21. Huttmacher DW. Scaffolds in tissue engineering bone and cartilage. *Biomaterials.* 2000;21(24):2529-2543. doi:10.1016/S0142-9612(00)00121-6.
22. Nam YS, Park TG. Porous biodegradable polymeric scaffolds prepared by thermally induced phase separation. *J Biomed Mater Res.* 1999;47(1):8-17. doi:10.1002/(SICI)1097-4636(199910)47:1<8::AID-JBM2>3.0.CO;2-L.
23. Akbarzadeh R, Yousefi A-M. Effects of processing parameters in thermally induced phase separation technique on porous architecture of scaffolds for bone tissue engineering. *J Biomed Mater Res Part B Appl Biomater.* 2014;102(6):1304-1315. doi:10.1002/jbm.b.33101.
24. Mikos AG, Sarakinos G, Leite SM, Vacanti JP, Langer R. Laminated three-dimensional biodegradable foams for use in tissue engineering. *Biomater Silver Jubil Compend.* 2006;14(5):93-100. doi:10.1016/B978-008045154-1.50013-7.
25. Yoshikawa H, Tamai N, Murase T, Myoui A. Interconnected porous hydroxyapatite ceramics for bone tissue engineering. *J R Soc Interface.* 2009;6 Suppl 3(December 2008):S341-S348. doi:10.1098/rsif.2008.0425.focus.
26. Bose S, Vahabzadeh S, Bandyopadhyay A. Bone tissue engineering using 3D printing. *Mater Today.* 2013;16(12):496-504. doi:10.1016/j.mattod.2013.11.017.
27. Dalton PD, Vaquette C, Farrugia BL, Dargaville TR, Brown TD, Huttmacher DW. Electrospinning and additive manufacturing: converging technologies.

- Biomater Sci.* 2013;1(1):1-27. doi:10.1039/c2bm00039c.
28. Wu G-H, Hsu S. Review: Polymeric-Based 3D Printing for Tissue Engineering. *J Med Biol Eng.* 2015;35(3):285-292. doi:10.1007/s40846-015-0038-3.
 29. Muerza-Cascante ML, Haylock D, Hutmacher DW, Dalton PD. Melt Electrospinning and Its Technologization in Tissue Engineering. *Tissue Eng Part B Rev.* 2014;0(0):1-16. doi:10.1089/ten.TEB.2014.0347.
 30. Hochleitner G, Jüngst T, Brown TD, et al. Additive manufacturing of scaffolds with sub-micron filaments via melt electrospinning writing. *Biofabrication.* 2015;7(3):35002. doi:10.1088/1758-5090/7/3/035002.
 31. Brown TD, Dalton PD, Hutmacher DW. Direct Writing By Way of Melt Electrospinning. *Adv Mater.* 2011;23(47):5651-5657. doi:10.1002/adma.201103482.
 32. Dalton PD, Vaquette C, Farrugia BL, Dargaville TR, Brown TD, Hutmacher DW. Electrospinning and additive manufacturing: converging technologies. *Biomater Sci.* 2013;1(2):171-185. doi:10.1039/C2BM00039C.
 33. Mammadov B, Sever M, Guler MO, Tekinay AB. Neural differentiation on synthetic scaffold materials. *J Biomater Sci Polym Ed.* 2013;1(11):1119-1137. doi:10.1039/c3bm60150a.
 34. Liu T, Houle JD, Xu J, Chan BP, Chew SY. Nanofibrous collagen nerve conduits for spinal cord repair. *Tissue Eng Part A.* 2012;18(9-10):1057-1066. doi:10.1089/ten.TEA.2011.0430.
 35. Pierschbacher MD, Ruoslahti E. Cell attachment activity of fibronectin can be duplicated by small synthetic fragments of the molecule. *Nature.* 1984;309(5963):30-33. doi:10.1038/309030a0.
 36. Petrie TA, Capadona JR, Reyes CD, García AJ. Integrin specificity and enhanced cellular activities associated with surfaces presenting a recombinant fibronectin fragment compared to RGD supports. *Biomaterials.* 2006;27(31):5459-5470. doi:10.1016/j.biomaterials.2006.06.027.
 37. Ruoslahti E, Pierschbacher MD. New perspectives in cell adhesion: RGD and integrins. *Science.* 1987;238(4826):491-497. doi:10.1126/science.2821619.
 38. Delforge D, Gillon B, Art M, Dewelle J. Design of a synthetic adhesion protein by grafting RGD tailed cyclic peptides on bovine serum albumin. ... *J Pept* 1998;(Figure 1):87-91. doi:10.1023/A:1008880124720.
 39. Bone A, Pluijm G Van Der, Robey PG, et al. Bone Sialoprotein Peptides Are Potent Inhibitors of Breast Cancer Cell. 1955;(31):1948-1955.
 40. Matsumura S, Hlil AR, Lepiller C, et al. Ionomers for proton exchange membrane fuel cells with sulfonic acid groups on the end-groups: Novel branched poly(ether-ketone)s. *Am Chem Soc Polym Prepr Div Polym Chem.* 2008;49(1):511-512. doi:10.1002/pola.
 41. Lyons J, Li C, Ko F. Melt-electrospinning part I: Processing parameters and geometric properties. *Polymer (Guildf).* 2004;45(22):7597-7603. doi:10.1016/j.polymer.2004.08.071.
 42. Zhang Q, Lu H, Kawazoe N, Chen G. Pore size effect of collagen scaffolds on cartilage regeneration. *Acta Biomater.* 2014;10(5):2005-2013. doi:10.1016/j.actbio.2013.12.042.
 43. JONES A, ARNS C, SHEPPARD A, HUTMACHER D, MILTHORPE B, KNACKSTEDT M. Assessment of bone ingrowth into porous biomaterials using MICRO-CT. *Biomaterials.* 2007;28(15):2491-2504. doi:10.1016/j.biomaterials.2007.01.046.
 44. Müller B, Deyhle H, Fierz FC, et al. Bio-mimetic hollow scaffolds for long bone replacement. *Proc SPIE.* 2009;7401(December 2015):74010D-74010D-13. doi:10.1117/12.825487.
 45. HABIBOVIC P, GBURECK U, DOILLON C, BASSETT D, VANBLITTERSWIJK C, BARRALET J. Osteoconduction and osteoinduction of low-temperature 3D printed bioceramic implants. *Biomaterials.* 2008;29(7):944-953. doi:10.1016/j.biomaterials.2007.10.023.

Appendix I

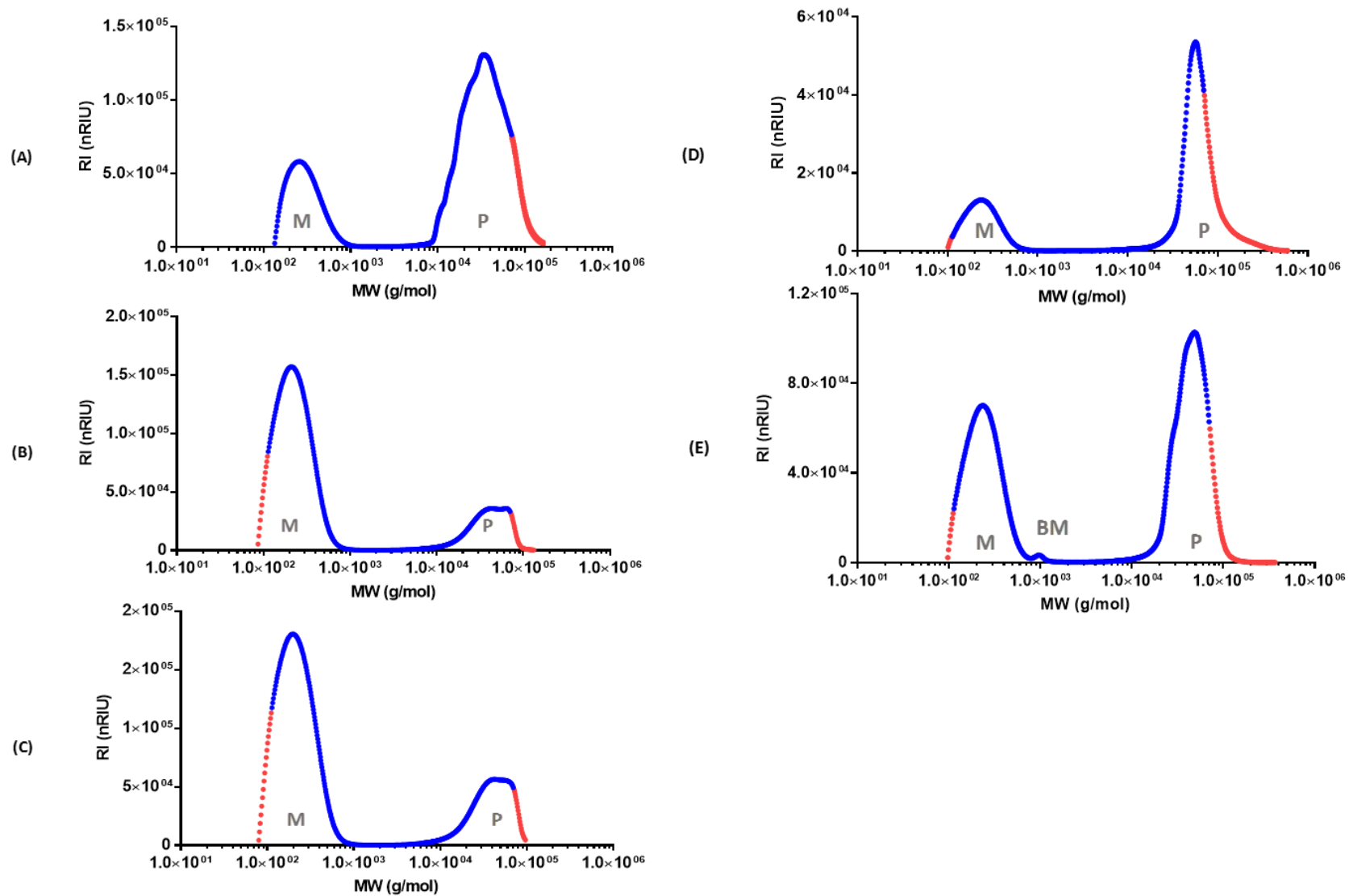


Figure 10 – SEC chromatograms of OEGMA 2 hour (except for (D), 24h) polymerization into pOEGMA by ARGET ATRP. (A) solution polymerization. (B) pOEGMA grafting from a PCL-initiated surface. (C) pOEGMA grafting from PCL-initiated electrospun fibers. (D) solution polymerization 24 hour assay. (E) p(OEGMA-co-biotin) grafting from PCL-initiated electrospun fibers. Blue points represent the molecular weights within the calibration range, and red points represent extrapolated estimates beyond the calibration. Peaks are identified as OEGMA monomer (M), pOEGMA brushes (P) and unreacted biotinylated monomer (BM).

Appendix II

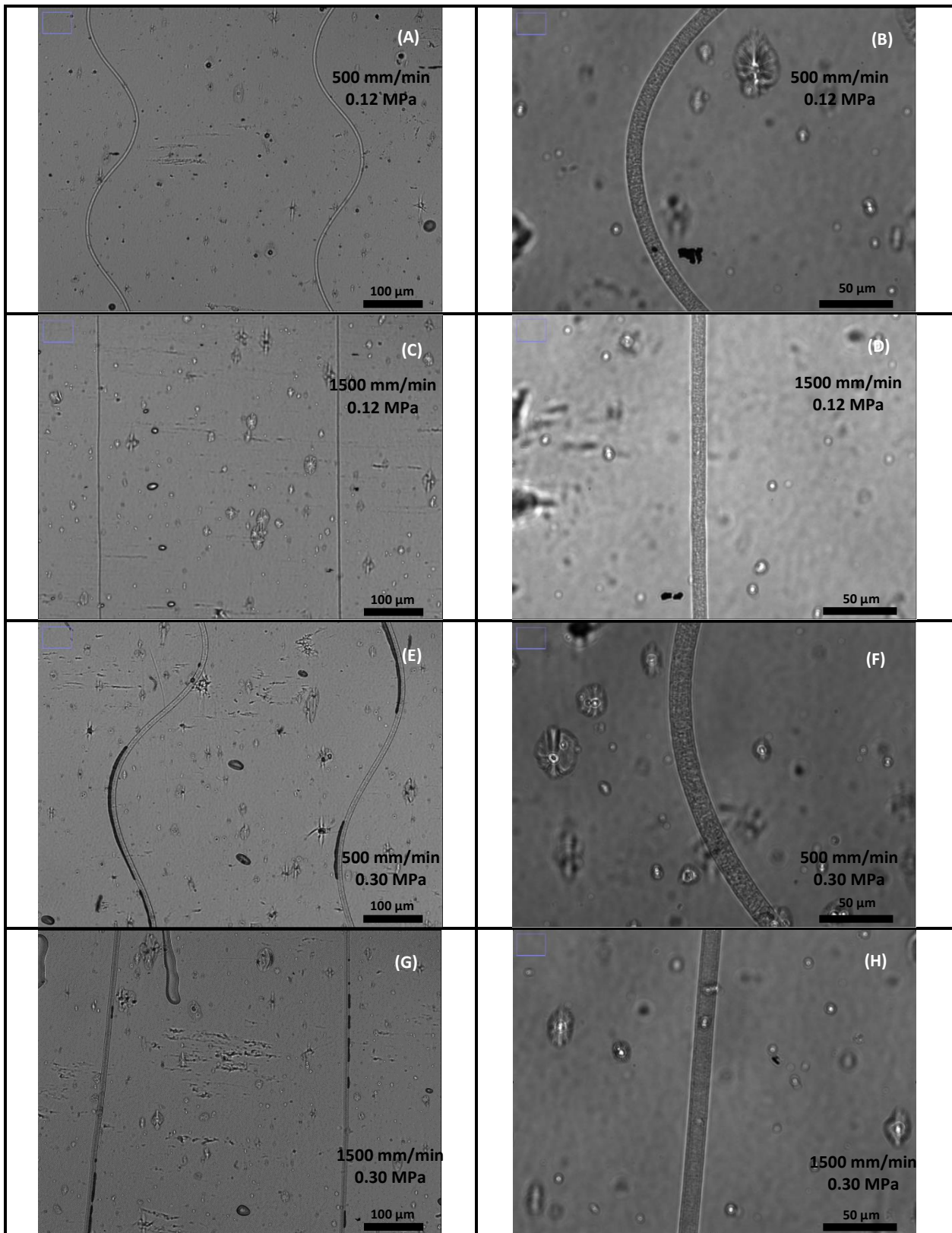


Figure 11 – FM photographs of single layer printed for 0.12 MPa and 500 mm/min: (A) 10x, (B) 40 x; and 1500 mm/min: (C) 10x, (D) 40 x. 0.30 MPa and 500 mm/min: (E) 10x, (F) 40 x; and 1500 mm/min: (G) 10x; (H) 40 x.

Appendix III

Table 1 – Analysis of the fibre deposition geometry (linear, wave-like, coil-like)

Pressure (Mpa)	Speed (mm/min)				
	500	750	1000	1250	1500
	Linear/wave-like/coil-like				
0.12	Wave-like	Wave-like	Linear	Linear	Linear
0.15	Wave-like	Wave-like	Linear	Linear	Linear
0.18	Wave-like	Wave-like	Linear	Linear	Linear
0.21	Wave-like	Wave-like	Linear	Linear	Linear
0.24	Wave-like	Wave-like	Linear	Linear	Linear
0.27	Wave-like	Wave-like	Linear	Linear	Linear
0.30	Wave-like	Wave-like	Linear	Linear	Linear

Table 2 – Average diameter measurements with the respective errors for each pressure and collector speed values. Cells are coloured with red gradients according to increases and decreases of values, in order to highlight the evolution of AFD with the two parameters in study.

Pressure (Mpa)	Speed (mm/min)					
	500		1000		1500	
	Average diameter $\pm \sigma$ (μm)					
0.12	8.4	$\pm 0,6$	6,9	$\pm 0,4$	5,7	$\pm 0,1$
0.15	9.3	$\pm 0,5$	7,2	$\pm 0,2$	7,7	$\pm 0,3$
0.18	9.9	$\pm 0,9$	8,7	$\pm 0,1$	7,7	$\pm 0,5$
0.21	11.2	$\pm 0,4$	8,8	$\pm 0,3$	8,5	$\pm 0,4$
0.24	11,9	$\pm 0,9$	9,0	$\pm 0,3$	10,1	$\pm 1,3$
0.27	11.5	$\pm 1,1$	11,2	$\pm 0,3$	9,3	$\pm 0,3$
0.30	12.1	$\pm 0,4$	11,3	$\pm 0,2$	10,7	$\pm 0,5$